Poeciliid Research

# Application of the hierarchical texture-descriptor tensor to histological muscle sections of *Poecilia reticulata*

Ştefan Ţălu

The Directorate of Research, Development and Innovation Management (DMCDI),
The Technical University of Cluj-Napoca, Cluj-Napoca, Romania.
Corresponding author: Ş. Ţălu, stefan.talu@auto.utcluj.ro

https://doi.org/10.67784/0096

**Abstract**. Histological assessment of fish skeletal muscle is mostly qualitative, and texture descriptors are usually reported at a single scale and averaged over orientation. This study applies a hierarchical texture-descriptor tensor, indexed by descriptor channel, Gaussian scale, orientation and region of interest (ROI), to two haematoxylin and eosin (HE) panels of guppy (*Poecilia reticulata*) muscle published under an open licence: a control panel and a panel from fish affected by *Tetrahymena pyriformis*. Ten channels were evaluated at four scales (1, 2, 4, 8 px) and four orientations, for one ROI (160 entries per image) and four ROIs (640 entries). The anisotropy index A and the texture axis were obtained exactly from the structure matrix and interpreted as circular statistics of the doubled gradient directions; a dilation-covariance relation was used to compare the panels at equal physical scale despite their different pixel sizes (0.75 and 0.96 μm $px^{-1}$). At s = 2 px, the control muscle was strongly oriented (A = 0.597, 95% CI 0.552-0.648), and its texture axis agreed within 4.2° with the orientation of the interfibre spaces segmented independently. The affected muscle was less oriented (A = 0.377, 95% CI 0.322-0.435); both values exceeded the 95th percentile of isotropic surrogates (≤ 0.034, P ≤ 0.005). At matched physical scales of 1-8 μm, A was 0.57-0.67 in the control and 0.35-0.47 in the affected muscle. The affected panel had a larger characteristic scale (9.9 versus 5.7 μm), a larger area of unstained space (37.5 versus 7.9%), lower co-occurrence contrast and energy and a higher second-derivative amplitude. The results are descriptive, rest on one panel per condition, and do not establish diagnostic value.
**Key words**: guppy, fish muscle histology, texture analysis, anisotropy, *Tetrahymena*.

**Introduction**. The guppy, *Poecilia reticulata* (Peters, 1859), is one of the most widely used poeciliids in ecotoxicology, aquaculture research and fish pathology, its responses to contaminants are evaluated in toxicity tests (Ţălu et al., 2012), and its tissues are routinely examined in haematoxylin and eosin (HE) sections (Martins et al., 2022). Skeletal muscle is among the organs damaged in ciliate infections: *Tetrahymena* species invade the skin and the underlying musculature of guppies and cause necrosis, inflammation and loss of the normal fibre architecture (Pimenta Leibowitz et al., 2009; Wang et al., 2024). In healthy fish muscle, fibres are compact and regularly arranged and are separated by thin endomysial spaces, whereas damaged muscle shows atrophy, rupture and disorganization of the fibres (Bernet et al., 1999; Strateva & Penchev, 2019; Wang et al., 2024). These changes are usually described qualitatively or, when fibres can be segmented, by fibre morphometry, which becomes unreliable when fibre outlines are lost.

Texture analysis describes the spatial variation of image intensity without segmentation, through statistics of intensity differences, co-occurrences, filter responses or scaling behaviour (Haralick et al., 1973; Gurcan et al., 2009; Ţălu, 2012a; Ghalati et al., 2022). Fractal, multifractal and lacunarity measures, which describe scale-dependent complexity, have been applied by the author to biological and medical images (Ţălu, 2012b; Ţălu, 2013a,b; Ţălu et al., 2013; Ţălu, 2026), including histological sections of the retina (Ştefănuţ et al., 2013), corneal and dental tissue surfaces (Ţălu et al., 2015;

Solaymani et al., 2019) and biological surfaces with a directional microstructure (Garczyk et al., 2017), and their use in aquaculture has recently been reviewed (Petrescu-Mag et al., 2026). Two difficulties limit the interpretation of such measures. First, texture depends jointly on the scale at which it is observed, the direction in which it is probed and the region over which it is summarized (Depeursinge, 2017); a single number per descriptor hides this dependence. Second, panels from published figures are often acquired at different magnifications, so that values compared in pixels refer to structures of different physical size.

A hierarchical descriptor tensor that keeps scale, orientation and region as separate indices of every measurement was introduced and applied to human and fish skeletal muscle in Ţălu (2027), where its readings were compared with synthetic reference fields. The present study applies the same tensor, without changes to its definitions, to two HE panels of guppy muscle published by Wang et al. (2024) under the Creative Commons Attribution (CC BY 4.0) licence: a control panel and a panel from fish affected by *Tetrahymena pyriformis*.

The aims of this research were (i) to describe how the tensor characterizes healthy and affected guppy muscle with one and four ROIs, (ii) to check the orientation index against an independent morphometric measurement, and (iii) to compare the two panels at matched physical scale. The study is a descriptive image analysis; it does not attempt to classify tissue or to estimate population-level effects.

**Theoretical Background**. Let $f$ be the z-scored luminance of a panel, $G_s = g_s * f$ its Gaussian scale-space at scale $s$ (standard deviation in pixels) (Lindeberg, 1998), and $\partial_\theta G_s = \cos\theta\ \partial_x G_s + \sin\theta\ \partial_y G_s$ the steerable directional derivative (Freeman & Adelson, 1991), with $\theta$ measured counter-clockwise from the horizontal and the $y$ axis pointing upward. For regions $W_1, \ldots, W_R$, the tensor of Ţălu (2027) is

$$\mathfrak{D} \in \mathbb{R}^{M\times K\times L\times R}, \qquad \mathfrak{D}_{mklr} = D_m(s_k, \theta_l, W_r) \tag{1}$$

with $M = 10$ channels (Table 2), $K = 4$ scales, $L = 4$ orientations and $R = 1$ or 4, i.e. 160 or 640 entries per image.

***Anisotropy and texture axis***. With the doubled-angle gradient field $z_s = \left(\partial_x G_s + i\ \partial_y G_s\right)^2$ and the regional mean $\langle\cdot\rangle_r$, the directional energy $D_2 = \langle(\partial_\theta G_s)^2\rangle_r$ is a quadratic form of the regional structure matrix $\mathbf{J} = \langle\nabla G_s \nabla G_s^{\mathrm{T}}\rangle_r$ (Bigün & Granlund, 1987; Ţălu, 2027):

$$D_2(\theta) = 1/2\,\langle|z_s|\rangle_r + 1/2\ \mathrm{Re}\left[\langle z_s\rangle_r e^{-2i\theta}\right] \tag{2}$$

so that the anisotropy index $A$ and the texture axis $\psi$ are

$$A = \frac{|\langle z_s\rangle_r|}{\langle|z_s|\rangle_r} = \frac{\lambda_+ - \lambda_-}{\lambda_+ + \lambda_-}, \qquad \psi = 1/2\arg\langle z_s\rangle_r + \frac{\pi}{2}\ (\mathrm{mod}\ \pi) \tag{3}$$

where $\lambda_+ \geq \lambda_-$ are the eigenvalues of $\mathbf{J}$. $A$ is the energy-weighted mean resultant length of the doubled gradient directions and $\psi$ is their circular mean rotated by $\pi/2$ (Mardia & Jupp, 2000): $A = 0$ when gradient energy is spread evenly over all directions and $A \to 1$ when all edges share one direction. Because $J_{xx} = D_2(0)$, $J_{yy} = D_2(\pi/2)$ and $J_{xy} = [D_2(\pi/4) - D_2(3\pi/4)]/2$, the four configured orientations determine $A$ and $\psi$ exactly, and the four entries obey the check $D_2(0) + D_2(\pi/2) = D_2(\pi/4) + D_2(3\pi/4)$. The index read directly from the four sampled values, $A_4$, satisfies $A/\sqrt{2} \leq A_4 \leq A$. For an equal-area partition into regions with indices $A_r$ and energies $E_r = \mathrm{tr}\,\mathbf{J}_r$,

$$A(\cup_r W_r) \leq \frac{\sum_r E_r A_r}{\sum_r E_r} \tag{4}$$

with equality only when the regional axes coincide (Ţălu, 2027); the gap between the two sides measures the disagreement between regional orientations.

***Dilation covariance and physical scale.*** If $f_c(\mathbf{x}) = f(c\mathbf{x})$ is the same tissue imaged with a pixel size $c$ times larger, then $G_s[f_c](\mathbf{x}) = G_{cs}[f](c\mathbf{x})$, hence

$$D_2(s,\theta;f_c) = c^2 D_2(cs,\theta;f), \qquad A(s;f_c) = A(cs;f), \qquad \psi(s;f_c) = \psi(cs;f) \tag{5}$$

Panels with pixel sizes $\Delta_1$ and $\Delta_2$ must therefore be compared at scales with $s_1\Delta_1 = s_2\Delta_2$; distribution-shape channels (kurtosis, entropy) transform like $A$, energy-type channels require the factor $c^2$ (or $c$ for first absolute moments), and co-occurrence and autocorrelation channels, whose offsets are proportional to $s$, transform like $A$ up to quantization and rounding. The scale-normalized energy $s^2 \operatorname{tr} \mathbf{J}_s$, whose maximum $s^*$ marks the dominant width of intensity transitions (Lindeberg, 1998), is reported in micrometres as $s^*\Delta$.

## Material and Method

***Image source and permission.*** The analysed images are panels F (muscle tissue of a control fish) and G (muscle tissue of diseased fish, described as atrophied and ruptured) of Figure 4 of Wang et al., (2024), which shows HE-stained sections of guppy liver, gill and muscle from an experimental infection with *Tetrahymena pyriformis* (scale bars 80 µm in panels F-I). The article is published open access under the Creative Commons Attribution 4.0 International licence (CC BY 4.0), which permits reuse and adaptation with appropriate credit; the source is cited in each figure caption and no further permission was required. Panels H and I, which show the parasite inside muscle at a field dominated by background, were not suitable for texture comparison and were not analysed. This study is a secondary analysis of published images and involved no animal experiments.

***Image preparation.*** The figure was downloaded at its full published resolution (2784 × 2478 px) and the panels were cropped at the white separators: F, 851 × 881 px; G, 898 × 656 px. The 80-µm scale bar measured 107 px in F and 83 px in G, giving pixel sizes of 0.748 and 0.964 µm px$^{-1}$ (ratio 1.29). The panel label and the scale bar were removed by fast-marching inpainting (Telea, 2004); the inpainted pixels formed 3.1% and 0.7% of the ROI of F and G. Luminance was computed as 0.299 R + 0.587 G + 0.114 B and z-scored over the panel; no contrast enhancement or colour normalization was applied. ROI = 1 was the central region after removing a 48-px margin (F, 755 × 785 px; G, 802 × 560 px), and ROI = 4 its four equal quadrants (1 upper left, 2 upper right, 3 lower left, 4 lower right). Filters were applied to the whole panel with reflective boundaries and aggregated over each ROI (Figure 1, Table 1).

***Descriptor tensor.*** The reference implementation of Ţălu (2027) was used: Gaussian scales s = 1, 2, 4, 8 px, orientations θ = 0, π/4, π/2, 3π/4, and the ten channels of Table 2, giving 10 × 4 × 4 × 1 = 160 entries per panel for ROI = 1 and 10 × 4 × 4 × 4 = 640 entries for ROI = 4. A and ψ were computed from Eq. (3). To compare the panels at equal physical scale, the tensor was also computed at the physical scales 1, 2, 4 and 8 µm (F: s = 1.34, 2.67, 5.35, 10.7 px; G: s = 1.04, 2.08, 4.15, 8.30 px). The characteristic scale s* was located on nine log-spaced scales (1-16 px) and refined by a parabola in log s.

***Uncertainty and reference for isotropy.*** Uncertainty of A and ψ was estimated by a block bootstrap (Künsch, 1989): ROI = 1 was divided into 8 × 8 blocks (ROI = 4: 6 × 6 blocks) resampled 1000 (500) times, and percentile 95% confidence intervals (CI) were reported. The reference for isotropy was a set of 200 surrogate images (100 for each quadrant) with the radially averaged Fourier amplitude of the panel and random phases (Theiler et al., 1992); these surrogates have no preferred direction but the same radial

spectrum, and the 95th percentile of A over them is the floor that an observed A should exceed (smallest attainable P = 1/201).

***Morphometric cross-check.*** As an independent reference for orientation, unstained interfibre spaces were delineated by fixed thresholds on the HSV representation (value > 0.80 and saturation < 0.20), followed by a one-pixel opening; objects of at least 40 px inside ROI = 1 were retained. Their long-axis orientation was summarized by the circular mean of the doubled angles weighted by elongation (1 − minor/major axis) and area, together with the resultant length R. Relationships between channels were examined with the Spearman correlation (Spearman, 1904) over the 128 entries of the two ROI = 4 tensors.

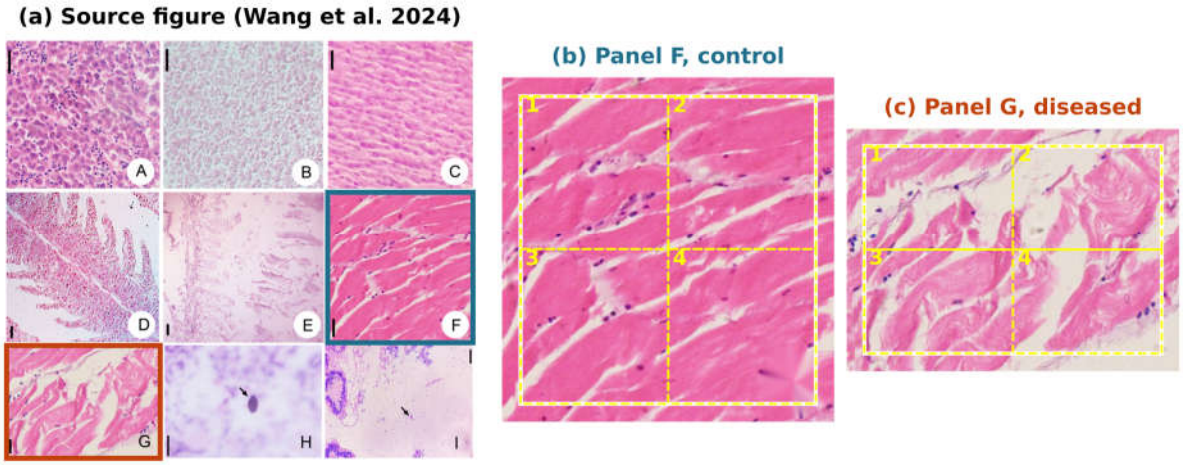



Figure 1. (a) Figure 4 of Wang et al (2024), reproduced under the CC BY 4.0 licence; panels F (control muscle, blue) and G (muscle of diseased fish, orange) were analysed. (b, c) Panels F and G after removal of the label and scale bar, with ROI = 1 (white) and the four ROIs of ROI = 4 (yellow, numbered).

Table 1

Analysed panels and analysis geometry (W × H in px)

| *Parameter* | *Panel F (control)* | *Panel G (diseased)* |
|---|---|---|
| Source | Wang et al (2024), Figure 4F | Wang et al (2024), Figure 4G |
| Panel size | 851 × 881 | 898 × 656 |
| 80-µm scale bar (px) | 107 | 83 |
| Pixel size (µm $px^{-1}$) | 0.748 | 0.964 |
| ROI = 1 (48-px margin) | 755 × 785 | 802 × 560 |
| ROI = 4, each quadrant | ≈ 377 × 392 | ≈ 401 × 280 |
| Inpainted share of ROI (%) | 3.1 | 0.7 |
| Luminance skewness / kurtosis | 1.10 / 4.70 | -0.23 / 2.42 |
| Unstained space in ROI (%) | 7.9 | 37.5 |

Table 2

The ten channels of the descriptor tensor (Ţălu, 2027)

| *Channel* | *Definition* | *Type* |
|---|---|---|
| D1 | mean of $\lvert\partial_\theta G_s\rvert$ | gradient amplitude |
| D2 | mean of $(\partial_\theta G_s)^2$ (directional energy) | gradient energy |
| D3 | kurtosis of $\partial_\theta G_s$ | distribution shape |
| D4 | Shannon entropy of $\partial_\theta G_s$ (32 bins, ± 4 SD, bits) | distribution shape |
| D5 | mean of $\lvert\partial^2_\theta G_s\rvert$ | second-derivative amplitude |
| D6-D9 | GLCM contrast, homogeneity, energy, correlation of $G_s$ (16 levels, offsets ± d, d = s along θ) | co-occurrence |
| D10 | normalized autocorrelation of $G_s$ at lag 2s along θ | spatial correlation |

## Results and Discussion

***Directional responses and the global tensor (ROI = 1).*** The directional derivatives (Figure 2) show that the control muscle is dominated by long, parallel boundaries between fibres, which respond strongly at θ = π/2 and 3π/4 and weakly at θ = π/4, i.e. across the fibres. In the affected muscle the boundaries are shorter, curved and interrupted by wide unstained spaces, and the fragments contain fine wavy striations. The complete tensors (Figure 3; all 160 + 640 entries per panel in Supplementary Table S1) show the expected decrease of the gradient channels with scale and a stronger orientation dependence in the control panel.

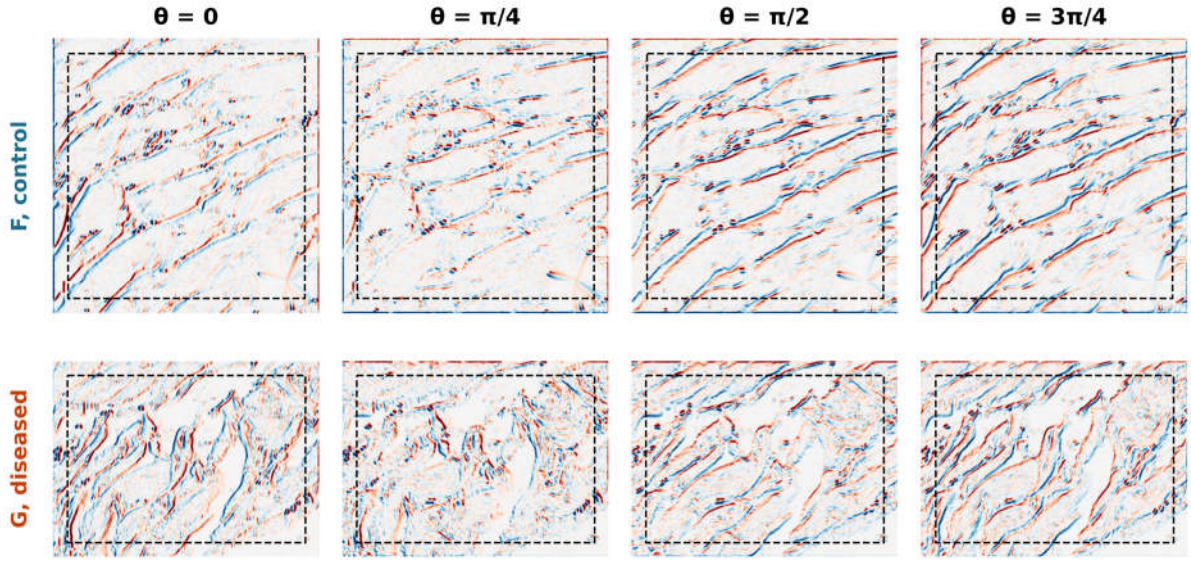



Figure 2. Directional derivative $\partial_\theta G$ at s = 2 px for the four configured orientations (red/blue = sign; dashed line: ROI = 1). Top: control muscle (F); bottom: muscle of diseased fish (G). Source images: Wang et al., (2024), CC BY 4.0.

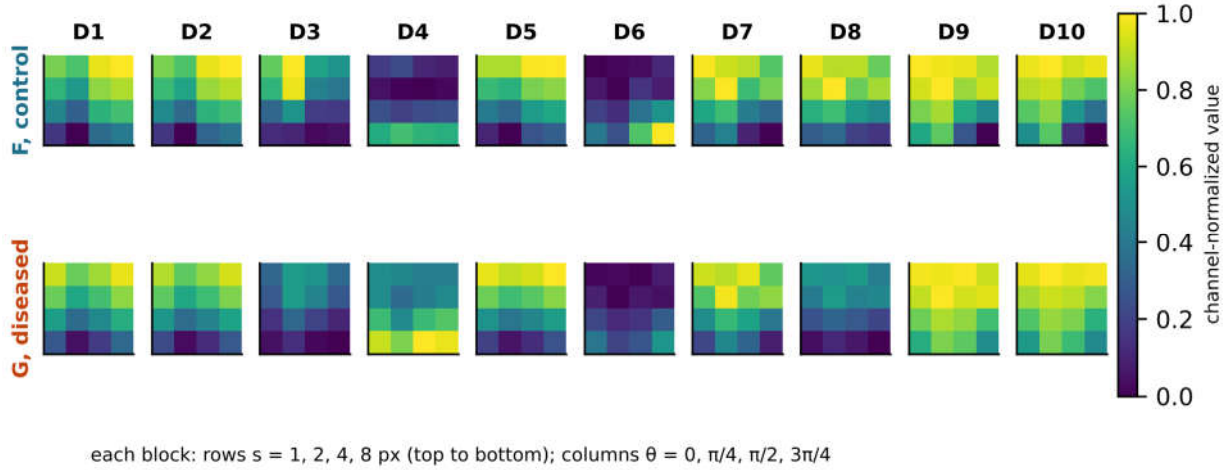



Figure 3. Descriptor tensor for ROI = 1: values of the ten channels at four scales and four orientations, normalized per channel over both panels (logarithmic for D1, D2 and D5).

Table 3

$D_2$ energy share at the four orientations, sampled index $A_4$, anisotropy index A from Eq. (3) with 95% bootstrap CI, 95th percentile of A for isotropic surrogates, and texture axis ψ (°, counter-clockwise from the horizontal) with 95% CI (ROI = 1)

| *Panel, s (px)* | *θ = 0* | *θ = π/4* | *θ = π/2* | *θ = 3π/4* | *$A_4$* | *A [95% CI]* | *Null 95th pct* | *ψ [95% CI]* |
|---|---|---|---|---|---|---|---|---|
| F, s = 1 | 0.176 | 0.132 | 0.324 | 0.368 | 0.471 | 0.557 [0.516, 0.597] | 0.009 | 28.9 [25.7, 32.2] |
| F, s = 2 | 0.175 | 0.121 | 0.325 | 0.379 | 0.515 | 0.597 [0.552, 0.648] | 0.011 | 29.8 [26.4, 33.2] |
| F, s = 4 | 0.174 | 0.108 | 0.326 | 0.392 | 0.566 | 0.643 [0.589, 0.697] | 0.016 | 30.9 [27.5, 34.3] |
| F, s = 8 | 0.177 | 0.098 | 0.323 | 0.402 | 0.608 | 0.675 [0.612, 0.732] | 0.028 | 32.1 [28.3, 36.0] |
| G, s = 1 | 0.274 | 0.167 | 0.226 | 0.333 | 0.331 | 0.344 [0.297, 0.398] | 0.010 | 52.9 [47.8, 58.7] |
| G, s = 2 | 0.278 | 0.160 | 0.222 | 0.340 | 0.360 | 0.377 [0.322, 0.435] | 0.014 | 53.7 [48.8, 59.5] |
| G, s = 4 | 0.286 | 0.153 | 0.214 | 0.347 | 0.388 | 0.414 [0.353, 0.478] | 0.021 | 55.2 [49.4, 60.8] |
| G, s = 8 | 0.297 | 0.143 | 0.203 | 0.357 | 0.430 | 0.469 [0.398, 0.543] | 0.034 | 56.8 [50.6, 62.6] |

The constraint $D_2(0) + D_2(\pi/2) = D_2(\pi/4) + D_2(3\pi/4)$ held to within $10^{-15}$ of the trace in all entries. $P \leq 0.005$ for every entry (no surrogate reached the observed A).

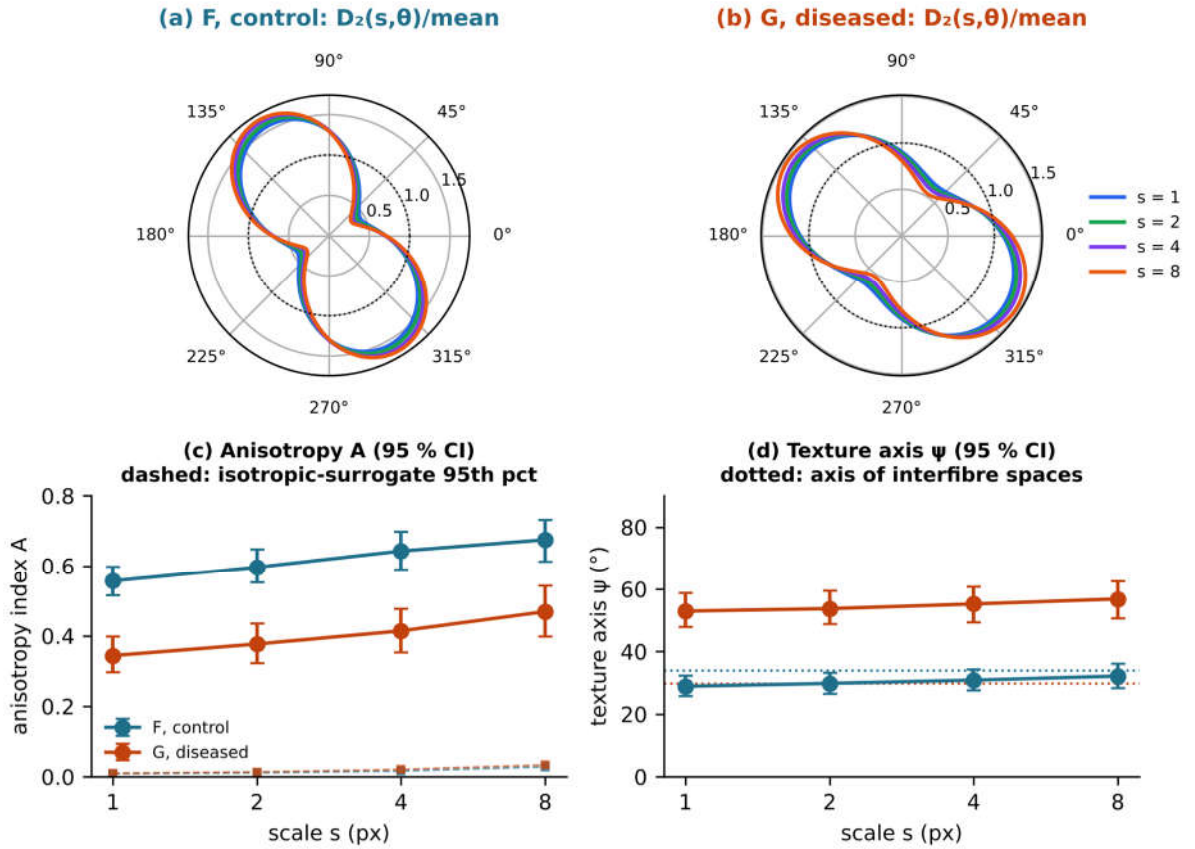



Figure 4. (a, b) Directional profiles $D_2(s,\theta)$/mean over θ reconstructed from the four tensor entries through Eq. (2), for s = 1, 2, 4 and 8 px; dotted circle: no directional preference. (c) Anisotropy index A against scale with 95% bootstrap CI; dashed: 95th percentile of A for isotropic surrogates. (d) Texture axis ψ with 95% CI; dotted lines: mean orientation of the interfibre spaces of each panel.

The two panels are clearly anisotropic, i.e. their gradient energy has a preferred direction, a property that scalar fractal or entropy descriptors do not capture (Garczyk et al., 2017; Petrescu-Mag et al., 2026). At s = 2 px, A = 0.597 (95% CI 0.552-0.648) in the control and 0.377 (0.322-0.435) in the affected muscle, against surrogate floors of 0.011 and 0.014 (Table 3, Figure 4); the confidence intervals do not overlap at any scale. In both panels A increases slightly with scale (control 0.557 to 0.675; affected 0.344 to 0.469), because coarser operators average out the fine, randomly oriented detail (nuclei, striations) and retain the dominant boundaries. The axes are stable across scales (control 28.9-32.1°; affected 52.9-56.8°). The axis values themselves are not comparable between panels, because the orientation of a section in the image depends on how the tissue was cut and photographed; only A, which is invariant to rotation, compares the

degree of orientation. The difference between $A_4$ and A (up to 0.08 in the control, whose axis lies between two sampled orientations) shows why A and ψ were computed from Eq. (3) rather than read from the four sampled values.

***Characteristic scale****.* The scale-normalized energy has an interior maximum in both panels (Figure 5): s = *7.69 px = 5.7 μm in the control and 10.31 px = 9.9 μm in the affected muscle. Because the panels have different pixel sizes, only the values in micrometres are comparable. The larger s* of the affected muscle indicates that its dominant intensity transitions are wider, in agreement with the wider unstained spaces and the larger, irregular fragments visible in Figure 1. In the control, s* ≈ 5.7 μm is of the order of the width of the narrow interfibre clefts, which are the dominant edges of a compact muscle.

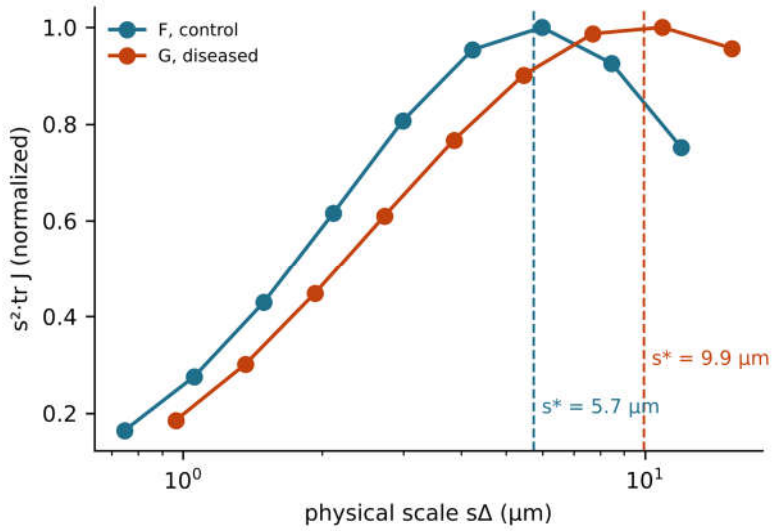



Figure 5. Scale-normalized energy $s^2 \cdot \mathrm{tr}\, J$ (mean over θ, ROI = 1, normalized to the maximum) against the physical scale sΔ; dashed lines: characteristic scale s*.

Table 4

Comparison of the panels at matched physical scale (ROI = 1, mean over θ): values F / G for scale-invariant quantities, and ratio G/F converted to physical units (Eq. 5) for the energy-type channels

| *Quantity* | *1 μm* | *2 μm* | *4 μm* | *8 μm* |
|---|---|---|---|---|
| A (Eq. 3) | 0.572 / 0.346 | 0.616 / 0.379 | 0.660 / 0.417 | 0.673 / 0.472 |
| D3 kurtosis | 15.1 / 10.8 | 11.8 / 9.93 | 6.62 / 6.75 | 4.4 / 4.49 |
| D4 entropy (bits) | 3.61 / 3.76 | 3.6 / 3.76 | 3.74 / 3.85 | 3.91 / 3.96 |
| D6 GLCM contrast | 0.26 / 0.254 | 0.686 / 0.296 | 1.14 / 0.641 | 2.03 / 0.99 |
| D7 GLCM homogeneity | 0.895 / 0.889 | 0.818 / 0.876 | 0.756 / 0.793 | 0.668 / 0.722 |
| D8 GLCM energy | 0.152 / 0.0979 | 0.126 / 0.0935 | 0.0911 / 0.0664 | 0.054 / 0.0413 |
| D9 GLCM correlation | 0.982 / 0.982 | 0.951 / 0.979 | 0.919 / 0.954 | 0.855 / 0.932 |
| D10 autocorrelation | 0.941 / 0.98 | 0.878 / 0.933 | 0.736 / 0.875 | 0.599 / 0.791 |
| D1 per μm (G/F) | 0.84 | 0.85 | 0.85 | 0.94 |
| D2 per μm² (G/F) | 0.60 | 0.62 | 0.65 | 0.82 |
| D5 per μm² (G/F) | 0.77 | 0.86 | 0.83 | 0.86 |

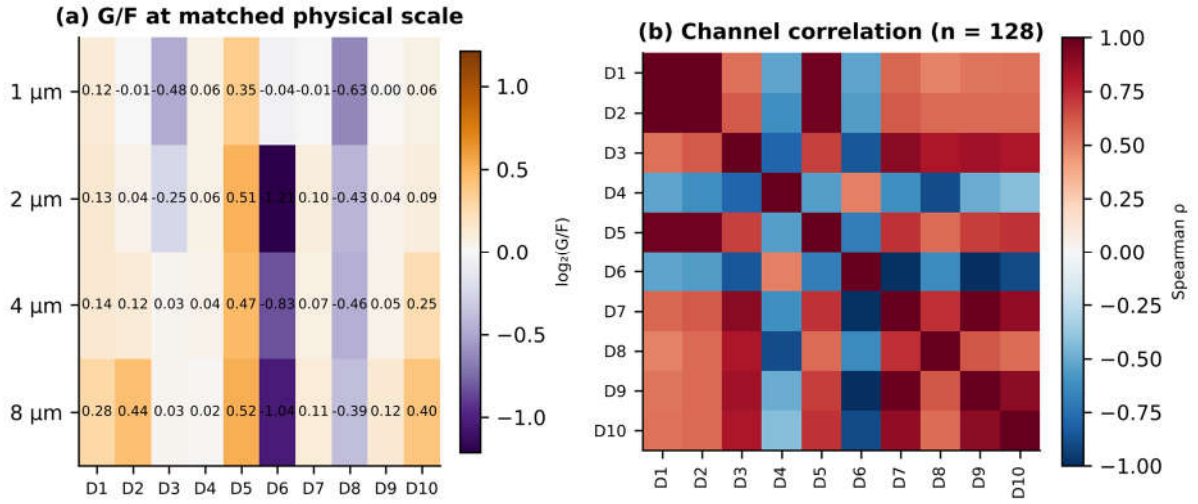



**Figure 6.** (a) $\log_2$ ratio G/F of the channel means at matched physical scales (energy-type channels shown in pixel units; see Table 4 for the physical conversion). (b) Spearman correlation between the ten channels over the 128 entries of the two ROI = 4 tensors.

***Comparison at matched physical scale.*** Because the pixel size of G is 1.29 times that of F, the panels were also compared at equal physical scales (Table 4, Figure 6). The difference in orientation persists: A is 0.57-0.67 in the control and 0.35-0.47 in the affected muscle at every scale from 1 to 8 µm. Converted to physical units, the gradient energy of the affected muscle is about 0.6-0.8 times that of the control and its first-derivative amplitude 0.85-0.95 times, and its second-derivative amplitude per µm² 0.77-0.87 times; the second-derivative channel is reduced less than the gradient energy, so the affected muscle has fewer strong edges per unit area but proportionally more fine curvature, in agreement with the wavy striations of the ruptured fibres. Co-occurrence energy (D8) is lower by 23-35% at all scales, and co-occurrence contrast (D6) is about half of the control value at 2-8 µm, while homogeneity, correlation and autocorrelation are higher at 2-8 µm. Because the luminance was z-scored over each panel, these co-occurrence channels describe local grey-level differences relative to the overall spread; in the affected panel the overall spread is dominated by the contrast between tissue and wide unstained spaces, so local differences are small relative to it. The kurtosis of the derivative is lower in the affected muscle at fine scales (1-2 µm), reflecting fewer isolated strong edges (nuclei and narrow clefts) on a smooth background.

Table 5

ROI = 4 at s = 2 px: $D_2$ shares, anisotropy index A with 95% bootstrap CI, 95th percentile of A for isotropic surrogates, and texture axis ψ (°) with 95% CI

| *ROI* | *θ = 0* | *θ = π/4* | *θ = π/2* | *θ = 3π/4* | *A [95% CI]* | *Null 95th pct* | *ψ [95% CI]* |
|---|---|---|---|---|---|---|---|
| F1 | 0.179 | 0.117 | 0.321 | 0.383 | 0.604 [0.549, 0.664] | 0.043 | 31.0 [27.6, 34.4] |
| F2 | 0.121 | 0.146 | 0.379 | 0.354 | 0.663 [0.609, 0.722] | 0.051 | 19.4 [15.4, 23.1] |
| F3 | 0.223 | 0.110 | 0.277 | 0.390 | 0.571 [0.492, 0.651] | 0.042 | 39.5 [33.7, 46.3] |
| F4 | 0.166 | 0.111 | 0.334 | 0.389 | 0.652 [0.570, 0.729] | 0.041 | 29.4 [26.2, 32.3] |
| G1 | 0.265 | 0.158 | 0.235 | 0.342 | 0.373 [0.262, 0.486] | 0.045 | 49.7 [40.6, 58.1] |
| G2 | 0.285 | 0.185 | 0.215 | 0.315 | 0.297 [0.187, 0.398] | 0.050 | 59.2 [46.7, 74.1] |
| G3 | 0.284 | 0.144 | 0.216 | 0.356 | 0.445 [0.358, 0.532] | 0.047 | 53.9 [44.4, 62.2] |
| G4 | 0.284 | 0.158 | 0.216 | 0.342 | 0.392 [0.312, 0.519] | 0.042 | 55.1 [47.9, 62.1] |

***Regional analysis (ROI = 4).*** All eight regional values of A exceed their surrogate floors (≤ 0.051) (Table 5, Figure 7). In the control, A ranges from 0.571 to 0.663 and the regional axes from 19.4° to 39.5°; in the affected muscle A ranges from 0.297 to 0.445, with the lowest A and the widest axis interval in ROI 2 (upper right), which contains a large unstained space (Figure 1c). The lower confidence bounds of the four control regions (0.492-0.609) lie above the upper bounds of affected ROIs 1 and 2 (0.486 and 0.398). The pooled index satisfies Eq. (4): 0.597 ≤ 0.617 in the control and 0.377 ≤ 0.379 in the affected muscle, where the energy-weighted means of the regional values

are on the right. The small gaps show that, within each panel, the regional axes agree closely and a single global value is an adequate summary of orientation; in the control the gap is larger (0.020) because ROI 2 and ROI 3 differ by 20° in axis.

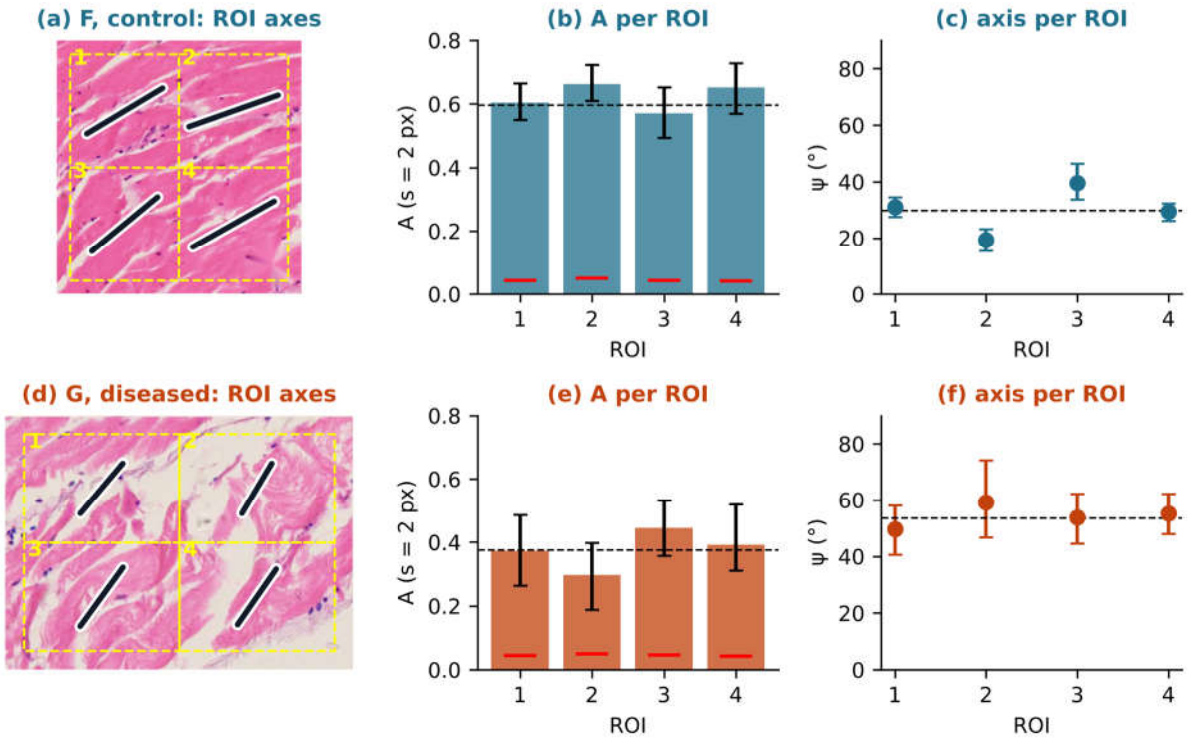



Figure 7. ROI = 4 at s = 2 px. (a, d) Texture axis of each ROI (line length proportional to A). (b, e) Anisotropy index A with 95% bootstrap CI; red marks: 95th percentile of A for isotropic surrogates; dashed line: A of ROI = 1. (c, f) Texture axis ψ with 95% CI; dashed line: axis of ROI = 1. Top: control (F); bottom: diseased (G). Source images: Wang et al (2024), CC BY 4.0.

Table 6

Coefficient of variation (%) of each channel across the four ROIs (s = 2 px, mean over θ)

| *Panel* | *D1* | *D2* | *D3* | *D4* | *D5* | *D6* | *D7* | *D8* | *D9* | *D10* |
|---|---|---|---|---|---|---|---|---|---|---|
| F (control) | 13.5 | 27.3 | 12.0 | 2.2 | 16.5 | 10.3 | 1.1 | 13.9 | 0.2 | 1.4 |
| G (diseased) | 10.6 | 21.2 | 22.9 | 2.1 | 9.4 | 17.8 | 2.3 | 18.9 | 0.4 | 1.9 |

The channels differ in spatial stability (Table 6). Entropy (D4), homogeneity (D7), correlation (D9) and autocorrelation (D10) vary by less than 2.5% between regions in both panels, whereas the energy-type channels (D2, D8) and kurtosis (D3) vary by 12-27%. The affected muscle has a higher regional variability of kurtosis (22.9 versus 12.0%) and of co-occurrence contrast (17.8 versus 10.3%), consistent with an uneven distribution of fragments and spaces.

***Local orientation and independent morphometric check***. The structure-tensor field (Figure 8) shows long domains of uniform orientation in the control and shorter, more variable domains in the affected muscle; the mean local coherence is 0.61 and 0.57. The segmented interfibre spaces (Figure 9, Table 7) provide an independent reference. In the control, the 66 spaces are narrow and elongated (median aspect ratio 3.22), strongly aligned (R = 0.89) and oriented at 34.0°, i.e. 4.2° from the tensor axis and close to the upper bound of its 95% CI (26.4-33.2°). In the affected muscle the spaces occupy 37.5% of the ROI, are less elongated (2.45) and less aligned (R = 0.61), and their mean orientation (29.8°) differs by 23.9° from the tensor axis. The tensor is dominated by the boundaries and internal striations of the remaining fibre fragments, whereas the large spaces between them are irregular; in damaged tissue the two measurements therefore describe different structures, and their disagreement is itself a marker of disorganization.

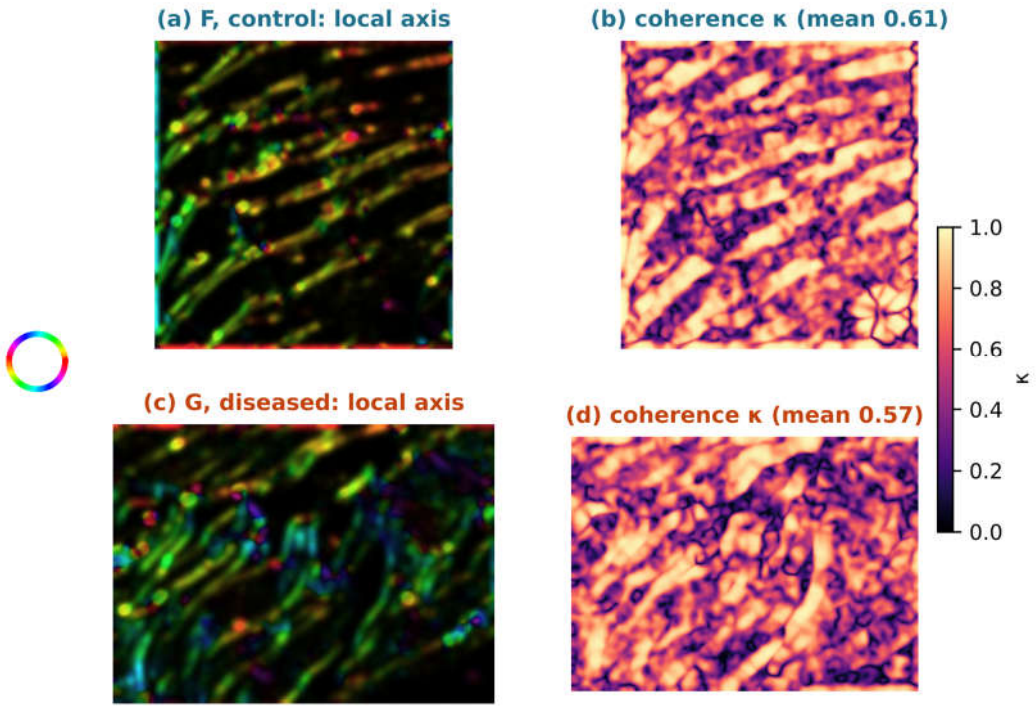



Figure 8. Structure-tensor representation at s = 2 px (Gaussian integration window σ = 8 px). (a, c) Local texture axis (hue; colour wheel on the left) modulated by energy and coherence (brightness). (b, d) Local coherence κ. Top: control (F); bottom: diseased (G).

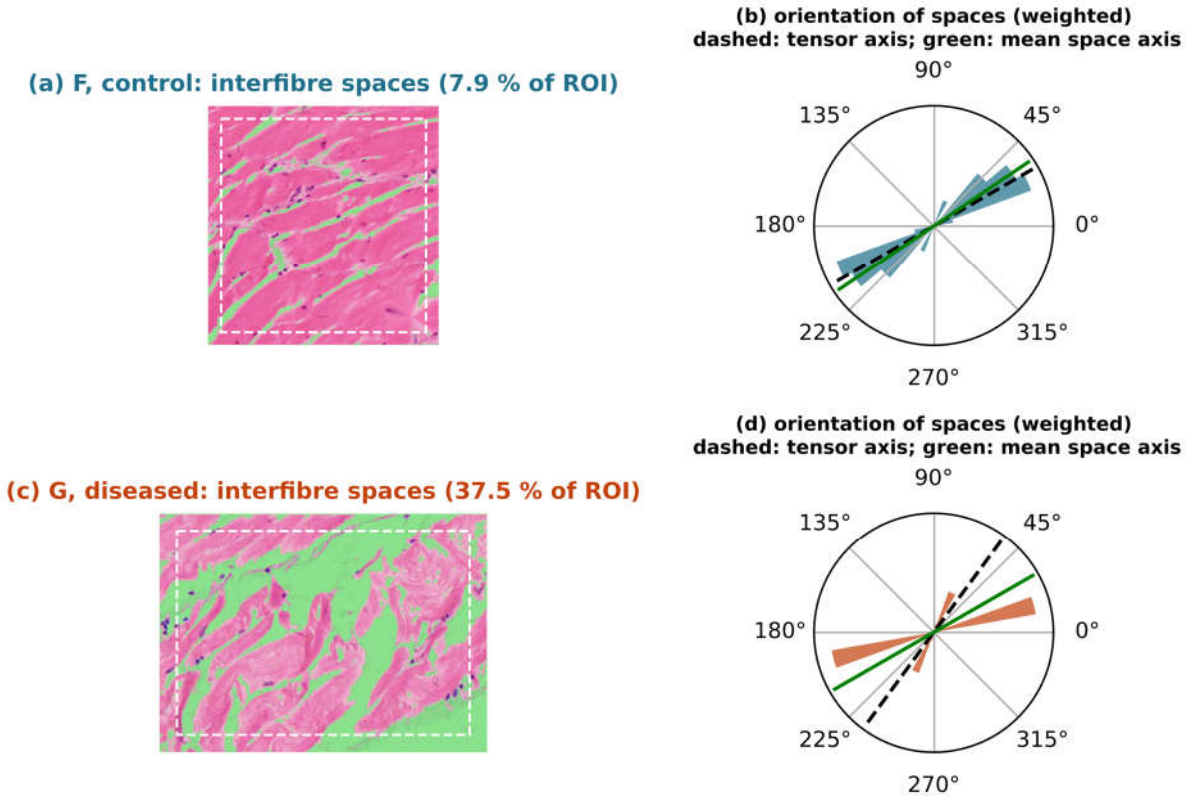



Figure 9. (a, c) Unstained interfibre spaces (green) segmented by fixed HSV thresholds; dashed line: ROI = 1. (b, d) Orientation distribution of the spaces weighted by elongation and area; dashed line: texture axis of the tensor (s = 2 px); green line: weighted mean orientation of the spaces. Source images: Wang et al (2024), CC BY 4.0.

Table 7

Interfibre spaces and texture axis of the tensor (ROI = 1, s = 2 px)

| *Panel* | *Spaces (n)* | *Area (%)* | *Median aspect ratio* | *Resultant length R* | *Space axis (°)* | *Tensor axis ψ (°)* | *\|Δ\| (°)* | *A* |
|---|---|---|---|---|---|---|---|---|
| F (control) | 66 | 7.9 | 3.22 | 0.89 | 34.0 | 29.8 | 4.2 | 0.597 |
| G (diseased) | 58 | 37.5 | 2.45 | 0.61 | 29.8 | 53.7 | 23.9 | 0.377 |

***Redundancy between channels.*** Over the 128 entries of the two ROI = 4 tensors, six channel pairs had $|\rho| \geq 0.95$: D1-D2 ($\rho = 0.99$); D1-D5 ($\rho = 0.96$); D2-D5 ($\rho = 0.96$); D6-D7 ($\rho = -0.99$); D6-D9 ($\rho = -1.00$); D7-D9 ($\rho = 0.98$) (Figure 6b). As in human and fish muscle (Ţălu, 2027), the gradient channels D1, D2 and D5 are practically equivalent, so one of them can represent the group. Co-occurrence contrast and correlation are almost perfectly anti-correlated here, in agreement with the identity $D_6 = 2\sigma_Q^2(1 - D_9)$ of Ţălu (2027), because the variance of the quantized image changes little between the entries of these two panels. Kurtosis (D3) and entropy (D4) carry partly independent information.

***Biological interpretation and limitations.*** The tensor separates two textures that correspond to the descriptions of the source study: a compact control muscle with long, parallel, strongly oriented fibre boundaries, and a disorganized affected muscle with atrophied and ruptured fibres, wide unstained spaces, a larger characteristic scale, weaker orientation and more fine curvature (Wang et al., 2024). These differences persist at matched physical scale, so they are not an effect of the different magnification of the panels. Compared with scalar fractal, multifractal and entropy descriptors proposed for aquaculture imaging (Petrescu-Mag et al., 2026), the tensor adds explicit orientation and scale indices, which here distinguished the two tissues more clearly than the intensity statistics alone, and it can be applied to the guppy tissues used in toxicological studies (Ţălu et al., 2012; Martins et al., 2022). The study has clear limits. Only one panel per condition was analysed, taken from a published figure (JPEG compression, unknown acquisition settings); the four ROIs are subsamples of one section and not biological replicates, so no statistical statement about groups of fish is possible. Panel labels and scale bars were inpainted. The two sections may differ in cutting plane, staining and illumination; z-scoring removes affine grey-level differences but non-linear channels (kurtosis, co-occurrence) remain sensitive to grey-level mapping. The segmentation of unstained spaces used fixed thresholds and is an approximate reference. A larger set of calibrated sections, several fish per group and a comparison with single-scale baseline descriptors are needed before any diagnostic use.

**Conclusions**. The hierarchical descriptor tensor of Ţălu (2027) was applied without changes to healthy and *Tetrahymena*-affected guppy muscle with one ROI (160 entries per panel) and four ROIs (640 entries). Interpreted through the circular statistics of doubled gradient directions and through its covariance under dilation, the tensor characterized the control muscle as a strongly oriented texture ($A \approx 0.6$) with a characteristic scale of about 6 µm and an axis that agreed with the orientation of the interfibre spaces, and the affected muscle as a less oriented texture ($A \approx 0.38$) with a larger characteristic scale ($\approx 10$ µm), larger unstained area, lower co-occurrence contrast and energy, and more fine curvature. These differences persisted at matched physical scale and in all four regions. The conclusions are descriptive and rest on one open-access panel per condition; they provide a reproducible quantitative description that can be extended to calibrated, replicated material.

**Acknowledgements**. The author thanks the authors of Wang et al., (2024) for publishing their histological images under an open licence.

**Conflict of Interest**. The author declares no conflict of interest.

**Data Availability**. The data used to support the findings of this study are available from the corresponding author upon request.

**Funding**. This research received no external funding.

## References

Bernet, D., Schmidt, H., Meier, W., Burkhardt-Holm, P., & Wahli, T. (1999). Histopathology in fish: Proposal for a protocol to assess aquatic pollution. *Journal of Fish Diseases, 22*(1), 25–34. https://doi.org/10.1046/j.1365-2761.1999.00134.x

Bigün, J., & Granlund, G. H. (1987). Optimal orientation detection of linear symmetry. In *Proceedings of the First International Conference on Computer Vision* (pp. 433–438).

Depeursinge, A. (2017). Multiscale and multidirectional biomedical texture analysis: Finding the needle in the haystack. In A. Depeursinge, O. S. Al-Kadi, & J. R. Mitchell (Eds.), *Biomedical Texture Analysis* (pp. 29–53). Academic Press.

Freeman, W. T., & Adelson, E. H. (1991). The design and use of steerable filters. *IEEE Transactions on Pattern Analysis and Machine Intelligence, 13*(9), 891–906.

Garczyk, Ż., Stach, S., Ţălu, Ş., Sobola, D., & Wróbel, Z. (2017). Stereometric parameters of butterfly wings. *Journal of Biomimetics, Biomaterials and Biomedical Engineering, 31*, 1–10.

Ghalati, M. K., Nunes, A., Ferreira, H., Serranho, P., & Bernardes, R. (2022). Texture analysis and its applications in biomedical imaging: A survey. *IEEE Reviews in Biomedical Engineering, 15*, 222–246. https://doi.org/10.1109/RBME.2021.3115703

Gurcan, M. N., Boucheron, L. E., Can, A., Madabhushi, A., Rajpoot, N. M., & Yener, B. (2009). Histopathological image analysis: A review. *IEEE Reviews in Biomedical Engineering, 2*, 147–171. https://doi.org/10.1109/RBME.2009.2034865

Haralick, R. M., Shanmugam, K., & Dinstein, I. (1973). Textural features for image classification. *IEEE Transactions on Systems, Man, and Cybernetics, SMC-3*(6), 610–621. https://doi.org/10.1109/TSMC.1973.4309314

Künsch, H. R. (1989). The jackknife and the bootstrap for general stationary observations. *The Annals of Statistics, 17*(3), 1217–1241. https://doi.org/10.1214/aos/1176347265

Lindeberg, T. (1998). Feature detection with automatic scale selection. *International Journal of Computer Vision, 30*(2), 79–116. https://doi.org/10.1023/A:1008045108935

Mardia, K. V., & Jupp, P. E. (2000). Directional statistics. John Wiley & Sons.

Martins, L. K. L., Lima-Faria, J. M., Guimarães, L. N., Silva, V. C., Moreira, P. C., & Sabóia-Morais, S. M. T. (2022). Co-exposure of iron oxide nanoparticles and glyphosate-based herbicide promote liver toxicity in guppy (*Poecilia reticulata*): A histochemical and ultrastructural approach. *Environmental Toxicology, 37*(9), 2244–2258. https://doi.org/10.1002/tox.23591

Petrescu-Mag, I. V., Ţălu, Ş., & Şahin, D. (2026). Fractal, multifractal and entropy-based approaches in aquaculture: An integrative review. *Aquaculture, Aquarium, Conservation & Legislation*, *19*(2), 882–898.

Pimenta Leibowitz, M., Ofir, R., Golan, Y., & Zilberg, D. (2009). *Tetrahymena* sp. infection in guppies, *Poecilia reticulata* Peters: Parasite characterization and pathology of infected fish. *Journal of Fish Diseases, 32*(10), 845–855. https://doi.org/10.1111/j.1365-2761.2009.01062.x

Solaymani, S., Elahi, S. M., Ghoranneviss, M., Shafiekhani, A., Kulesza, S., Ţălu, Ş., Bramowicz, M., Hantehzadeh, M. R., & Beryani Nezafat, N. (2019). The relation between structural, rugometric and fractal characteristics of hard dental tissues at micro and nano levels. *Microscopy Research and Technique, 82*(4), 421–428. https://doi.org/10.1002/jemt.23183

Spearman, C. (1904). The proof and measurement of association between two things. *The American Journal of Psychology, 15*(1), 72–101. https://doi.org/10.2307/1412159

Ştefănuţ, A. C., Ţălu, Ş., Miclăuş, V., Mureşan, A., Moldovan, R., & Szabo, B. (2013). Postnatal development of the retina in rats exposed to hyperoxia: A fractal analysis. *ISRN Biomedical Imaging, 2013*, Article 589327. https://doi.org/10.1155/2013/589327

Strateva, M., & Penchev, G. (2019). Histological discrimination of fresh from frozen/thawed carp (*Cyprinus carpio*). *Bulgarian Journal of Veterinary Medicine, 24*(3):434-441. https://doi.org/10.15547/bjvm.2019-0113

Telea, A. (2004). An image inpainting technique based on the fast-marching method. *Journal of Graphics Tools, 9*(1), 23–34. https://doi.org/10.1080/10867651.2004.10487596

Theiler, J., Eubank, S., Longtin, A., Galdrikian, B., & Farmer, J. D. (1992). Testing for nonlinearity in time series: The method of surrogate data. *Physica D: Nonlinear Phenomena, 58*(1–4), 77–94. https://doi.org/10.1016/0167-2789(92)90102-S

Ţălu, Ş. (2012a). Texture analysis methods for the characterisation of biological and medical images. *Extreme Life, Biospeology & Astrobiology*, *4*(1), 8-12.

Ţălu, Ş. (2012b). Mathematical methods used in monofractal and multifractal analysis for the processing of biological and medical data and images. *Animal Biology & Animal Husbandry*, *4*(1), 1–4.

Ţălu, Ş. (2013a). Multifractal geometry in analysis and processing of digital retinal photographs for early diagnosis of human diabetic macular edema. *Current Eye Research, 38*(7), 781–792. https://doi.org/10.3109/02713683.2013.779722

Ţălu, Ş. (2013b). Characterization of retinal vessel networks in human retinal imagery using quantitative descriptors. *Human & Veterinary Medicine, 5*(2), 52–57.

Ţălu, Ş. (2026). A unified fractal-entropy-manifold framework for multi-modal medical image fusion. *Human & Veterinary Medicine*, *18*(1), 40–52.

Ţălu, Ş. (2027). A hierarchical tensor framework for quantitative multiscale and multidirectional biomedical texture characterization. *Human & Veterinary Medicine, 19*(1). https://doi.org/10.67784/0095

Ţălu, Ş., Petrescu-Mag, I. V., & Păsărin, B. (2012). Investigation on acute toxicity of lindane in guppies, *Poecilia reticulata* Peters, 1859. *Poeciliid Research*, *2*(1), 9–14.

Ţălu, Ş., Stach, S., Sueiras, V., & Ziebarth, N. M. (2015). Fractal analysis of AFM images of the surface of Bowman's membrane of the human cornea. *Annals of Biomedical Engineering, 43*(4), 906–916. https://doi.org/10.1007/s10439-014-1140-3

Ţălu, Ş., Vlăduţiu, C., Popescu, L. A., Lupaşcu, C. A., Vesa, Ş. C., & Ţălu, S. D. (2013). Fractal and lacunarity analysis of human retinal vessel arborisation in normal and amblyopic eyes. *Human & Veterinary Medicine*, *5*(2), 45–51.

Wang, J., Wang, X., Liu, L., Wang, X., Wang, J., Zheng, Y., Wang, L., & Pan, X. (2024). Analyzing the interaction between *Tetrahymena pyriformis* and bacteria under different physicochemical conditions when infecting guppy using the eDNA method. *Animals, 14*(15), Article 2194. https://doi.org/10.3390/ani14152194

Received: 12 September 2026. Accepted: 28 October 2026. Published online: 28 October 2026.
Author:
Ştefan Ţălu, The Directorate of Research, Development and Innovation Management (DMCDI), The Technical University of Cluj-Napoca, Constantin Daicoviciu St., no. 15, Cluj-Napoca 400020, Cluj County, Romania, e-mail: stefan.talu@auto.utcluj.ro; stefan.talu1@gmail.com https://orcid.org/0000-0003-1311-7657
This is an open-access article distributed under the terms of the Creative Commons Attribution License, which permits unrestricted use, distribution and reproduction in any medium, provided the original author and source are credited.
How to cite this article:
Ţălu, Ş. (2026). Application of the hierarchical texture-descriptor tensor to histological muscle sections of *Poecilia reticulata*. *Poeciliid Research, 16*(1), 62-74. https://doi.org/10.67784/0096